energies

MDPI

Article

Transient Thermal Response of a Gravity Compressed Air Energy Storage Reservoir with Coupled Boundary Motion and Gas–Solid Heat Transfer

Zhengjie Sun [1], Yaan Hu [1,*], Linrui Ma [2], Xiaodong Wang [1], Weixiang Ni [1,*] and Xing'en Wang [3]

[1] Nanjing Hydraulic Research Institute, Nanjing 210029, China
[2] College of Energy and Electrical, Qinghai University, Xining 810036, China
[3] PowerChina Guiyang Engineering Corporation Limited, Guiyang 550081, China
* Correspondence: yahu@nhri.cn (Y.H.); wxni@nhri.cn (W.N.)

Abstract

In gravity-compressed air energy storage (G-CAES), a gravity-loaded pressure cylinder adjusts the reservoir volume to maintain the air pressure near its design value over the effective stroke. To investigate the coupling between cylinder motion and gas–solid heat transfer, a two-dimensional transient model was developed that couples compressible air flow, conjugate heat transfer, and cylinder dynamics. Simulated air temperatures were compared with measurements at the corresponding location at the bottom of a 1:10-scale reservoir. Initial charging proceeded through constant-volume pressurization before cylinder lift-off and near-isobaric, variable-volume charging thereafter. At lift-off, the expanding air did work on the moving boundary, contributing to the rapid decline in mean reservoir air temperature after its peak. At an inlet mass flow rate of 4.30 kg/s, increasing the inlet temperature from 293.15 to 333.15 K raised the peak mean air temperature by 40.41 K and shortened the time to peak from 2.64 to 2.36 min. At an inlet temperature of 333.15 K, increasing the inlet mass flow rate from 2.15 to 12.90 kg/s raised the peak by 21.31 K and shortened the time to peak from 4.72 to 0.78 min. Over 50 operating cycles, the mean end-of-cycle steel-lining temperature increased monotonically, with smaller increments in later cycles. The differences between successive cycles at matching phases decreased for both the mean air and steel-lining temperatures, indicating an approach to a repeatable periodic thermal response under the conditions investigated. The transient temperature fields can inform thermal load management and provide temperature inputs for subsequent steel-lining thermal stress analyses.

Keywords: G-CAES; isobaric compression; numerical simulation; air reservoir; dynamic heat transfer characteristics

Academic Editor: Andrea De Pascale

Received: 22 October 2026
Revised: 19 November 2026
Accepted: 23 November 2026
Published: 27 November 2026

Copyright: © 2026 by the authors. Licensee MDPI, Basel, Switzerland. This article is an open access article distributed under the terms and conditions of the Creative Commons Attribution (CC BY) license.

1. Introduction

The continued expansion of installed wind and photovoltaic power capacity has increased the need for power systems to balance supply and demand flexibly across time periods [1]. In compressed air energy storage (CAES) systems, off-peak electricity or surplus renewable electricity drives compressors, and the compressed air is stored at high pressure in underground caverns or aboveground pressure vessels. During periods of peak demand, the stored air is released to drive an expander and generate electricity [2,3]. The recovery and utilization of compression heat directly affect round-trip efficiency, while the evolution of temperature and pressure within the air reservoir governs the air supply conditions upstream of the expander and influences operational stability.

In conventional diabatic CAES, air undergoes multistage compression with intercooling during charging, and the heat of compression is rejected to the environment. During discharge, the high-pressure air released from the reservoir is heated by supplementary fuel combustion before entering the expander. The Huntorf plant in Germany and the McIntosh plant in the United States are representative installations of this type. At McIntosh, a recuperator uses waste heat from the expander exhaust to preheat the air released from the reservoir, thereby reducing the fuel required for supplementary heating [3]. To eliminate reliance on fossil fuels for reheating, advanced adiabatic compressed air energy storage (AA-CAES) incorporates a thermal energy storage subsystem that recovers and stores compression heat. During charging, the hot compressed air transfers heat to the storage medium before entering the reservoir. During discharge, the air released from the reservoir is reheated using the stored thermal energy before entering the expander to produce work [4]. Geissbühler et al. [4] used a packed bed of rocks in a pilot-scale AA-CAES plant. Air flowed through the voids between the rocks and exchanged heat with them directly, enabling sensible heat storage and recovery. To limit the decline in outlet air temperature during the later stages of discharge from the sensible heat store, Becattini et al. [5] supplemented the rock bed with a latent heat storage unit containing an encapsulated phase change material (PCM). Their experiments showed that latent heat release helped sustain the outlet air temperature during discharge. Because PCMs typically have low intrinsic thermal conductivity, fins can increase the heat transfer area and provide highly conductive paths into the material. Bouzennada et al. [6] numerically investigated tree-shaped fins placed in the lower part of a thermal storage enclosure. Their results showed that the fins substantially enhanced heat transfer in the conduction-dominated region, shortening the melting time of the nano-enhanced phase change material. Upstream compression heat recovery thus determines the temperature of the high-pressure air entering the reservoir. Within the reservoir, subsequent temperature evolution depends on the charging and discharging flows and on heat exchange between the air and the enclosing structure.

The means of regulating the air reservoir volume also determines how the storage pressure varies during operation. In a conventional constant-volume reservoir, the accumulation of air during charging causes a substantial pressure rise, and the withdrawal of air during discharge causes a corresponding pressure drop. During hold periods, gas–solid heat transfer can also induce pressure variations by changing the air temperature. To meet the expander's rated inlet pressure, some constant-volume systems throttle the air during discharge, resulting in substantial exergy destruction [7]. Isobaric air storage accommodates changes in air mass and temperature by dynamically adjusting the storage volume, thereby keeping the pressure close to its target value over the effective operating range. Existing isobaric or near-isobaric configurations include hydrostatic compensation using the water head from a surface reservoir [8], flexible underwater air storage that relies on the hydrostatic pressure of a natural water body [9–11], and active fluid compensation using water or carbon dioxide to vary the volume available to the stored air [7]. Other configurations regulate pressure by exploiting the volume change during vaporization and condensation and the saturation vapor pressure of a volatile working fluid [12,13], or by applying a mechanical load to a moving boundary through a spring-actuated scissor mechanism [14] or a gravity-loaded piston [15]. In gravity-compressed-air energy storage (G-CAES), a gravity-loaded pressure cylinder regulates the reservoir volume. During charging, the gas pressure lifts the cylinder, increasing the storage volume. During discharge, the cylinder descends under gravity, reducing the storage volume. Within the effective stroke, the force generated by the pressure differential across the cylinder approximately balances the combined weight of the cylinder and the ballast blocks, maintaining the storage pressure close to its design value.

Experimental and computational fluid dynamics studies have examined transient variations in temperature and pressure, as well as spatial temperature distributions, in different types of air storage facilities. For aboveground constant-volume storage, Guo et al. [16] investigated the effects of operating pressure range, mass flow rate, and vessel dimensions on the temperature and pressure responses of a glass-fiber-reinforced composite air storage vessel. They found that vessel diameter appreciably affected the uniformity of the air temperature distribution during charging. Liu et al. [17] developed a two-dimensional axisymmetric CFD model and validated it against operating data from the Huntorf plant. They used the model to investigate how inlet air temperature, flow rate, and the height-to-diameter ratio affect the temperature field in an engineered air reservoir and to explain the formation of a localized high-temperature region near the bottom during charging.

In underground caverns, the thermal response of the stored air is also strongly influenced by heat transfer through the lining and surrounding rock. Rutqvist et al. [18] developed a coupled thermodynamic and geomechanical model to analyze changes in air temperature, air pressure, and stresses in the surrounding rock during cyclic operation of lined rock caverns. Forced convection dominates during charging and discharging, whereas natural convection driven by the temperature difference between the air and the cavern walls prevails during hold periods. To account for mixed convection, Liao et al. [19] incorporated a modified heat transfer coefficient dependent on the Reynolds and Rayleigh numbers into a cavern thermodynamic model, substantially improving the accuracy of air temperature predictions during hold periods. Menéndez et al. [20] developed a three-dimensional CFD model of a lined mine drift to examine variations in air temperature and pressure and heat transfer through the drift walls over ten consecutive charge–discharge cycles. Di et al. [21] incorporated gas–solid heat transfer and air leakage into a coupled thermo-hydro-mechanical analysis of a rock cavern. During long-term cyclic operation, the range of air temperature fluctuations gradually stabilized, while the cavern wall temperature continued to rise slowly. This finding indicates that assessing whether the system has reached a periodic thermal steady state requires tracking the temperatures of both the stored air and the solid boundaries. In liquid-piston systems, movement of the gas–liquid interface changes the gas volume, and the gas exchanges heat with both the liquid and the solid walls. Odukomaiya et al. [22,23] investigated the use of spray droplets to enhance direct gas–liquid heat transfer and moderate temperature variations during compression and expansion. They also experimentally evaluated near-isothermal, near-isobaric energy storage using a condensable working fluid. Khaljani et al. [24] combined compression experiments with three-dimensional two-phase CFD simulations, using the volume-of-fluid (VOF) method to track the moving gas–liquid interface. They examined how the geometry of internal parallel aluminum plates and the compression rate affected the flow field, temperature distribution, and compression efficiency.

Although these studies have characterized flow and heat transfer in constant-volume reservoirs, underground caverns, and liquid-piston systems, their models have limited applicability to the transient thermodynamics of G-CAES air reservoirs. In the constant-volume CFD model of Liu et al. [17], the height-to-diameter ratio varied across cases, with the gas domain held fixed throughout each simulation. In the system-level analysis by Zhang et al. [15], the gravity-based air reservoir was represented as a component with constant storage pressure and a prescribed outlet temperature. Their analysis focused on the effects of storage pressure and shaft radius on system efficiency and energy storage cost. To resolve the internal flow and heat transfer in a G-CAES air reservoir, this study develops a two-dimensional planar transient numerical model that couples compressible flow and gas–solid conjugate heat transfer with the equation of verti-

cal motion and the stroke constraints of the pressure cylinder. An arbitrary Lagrangian–Eulerian (ALE) moving-mesh method updates the gas domain as the cylinder moves. Within a single charging process, the model resolves the transition from constant-volume pressurization before cylinder lift-off to near-isobaric charging at variable volume after lift-off. As the cylinder rises, the air performs work on the moving boundary, and the cylinder displacement changes the area of the air–steel lining interface. Moving-boundary work and gas–solid heat transfer across this changing interface jointly govern the temperature evolution of the stored air.

The numerical model is validated by comparing the simulated air temperature at the reservoir bottom with measurements taken at the corresponding location in a 1:10-scale experimental facility. The model is then used to examine how inlet air temperature and mass flow rate affect the magnitude and timing of the peak mean reservoir air temperature during initial charging. The coupled temperature evolution of the stored air and the steel lining is also analyzed over 50 consecutive charge–discharge cycles. The simulated temperatures inform the selection of operating parameters and the assessment of structural thermal loads for this G-CAES reservoir configuration.

2. System Description

G-CAES is a novel compressed air energy storage system based on a gravity-loaded, constant-pressure air reservoir. Its main configuration, shown in Figure 1, comprises a compression subsystem, a heat exchange and thermal energy storage subsystem, a gravity-based air storage subsystem, and an expansion and power generation subsystem. The defining feature of G-CAES is its constant-pressure air storage mechanism, which can be integrated with different aboveground thermodynamic cycle configurations. Figure 1 illustrates an advanced adiabatic G-CAES system.

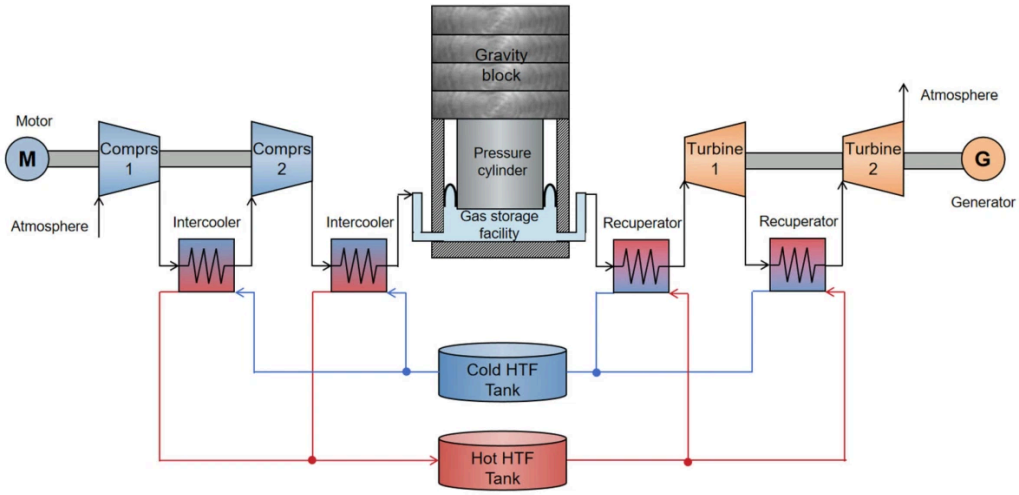


Figure 1. Process flow diagram of the G-CAES system. Black arrows indicate the air-flow direction, while red and blue lines with arrows indicate the hot and cold heat transfer fluid (HTF) flow paths, respectively. The hatched area represents the steel lining.

During charging, off-peak electricity or renewable electricity drives multistage compressors to compress ambient air. This process converts electrical energy into the pressure energy and thermal energy of the air. To maximize system exergy efficiency, compression heat is recovered from the air through interstage heat exchangers and stored in the hot heat transfer fluid (HTF) tank of the thermal energy storage subsystem. Cooling reduces the specific volume of the air before it enters the next compression stage, thereby lowering the subsequent compression work. The recovered compression heat is

retained for air reheating during subsequent discharge. The conditioned high-pressure air is delivered to the air reservoir.

During air storage, the pressure force exerted by the incoming high-pressure air drives the gravity blocks vertically upward. During discharge, the blocks descend under gravity in a controlled manner, maintaining a constant reservoir pressure. Most of the pneumatic energy supplied to the reservoir is converted into the gravitational potential energy of the gravity blocks, while a smaller fraction remains as the internal energy of the air. The use of gravitational potential energy avoids the time-dependent pressure decay associated with energy stored through gas compression and involves no substantial energy dissipation during storage, providing stable mechanical boundary conditions for long-duration energy storage. A gap is maintained between the pressure cylinder and the steel lining to accommodate a sealing membrane anchored to both components. The membrane ensures gas tightness while preventing direct contact between the pressure cylinder and the lining, thereby avoiding substantial frictional energy losses during operation.

In the engineering design of G-CAES, the internal reservoir pressure is determined by mechanical equilibrium. The pressure regulation mechanism is governed by the relationship among the total mass of the gravity blocks, the effective pressure-bearing area, and the target operating pressure. The rated operating pressure is primarily set by adjusting the gravitational load configuration. Changing the stacking height of the gravity blocks or selecting filling materials with different densities can substantially alter their total mass. Increasing or decreasing this load directly changes the force per unit area at the piston base, thereby regulating the internal storage pressure. The internal diameter of the air reservoir is another important parameter for pressure regulation. Optimizing the effective piston area during the design stage enables the required pressure to be achieved when the available gravitational load is limited.

During energy discharge through expansion, constant-pressure air released from the reservoir passes through the recuperators, where it absorbs the thermal energy stored in the HTF tank. The resulting high-temperature, high-pressure air enters the turbine expanders to drive the generator. The constant-pressure conditions maintained by the gravity piston allow the turbines to operate at their rated inlet pressure throughout discharge, avoiding the throttling exergy losses encountered by variable-pressure storage systems during the initial discharge stage.

Figure 2 shows the configuration of the full-scale G-CAES air reservoir and the energy transfer paths during charging. The main components are the steel shaft lining, the pressure cylinder, the flexible sealing membrane, and the gravity blocks mounted above the cylinder. The shaft inner diameter, cylinder outer diameter, and design stroke are 6 m, 5 m, and 21 m, respectively. The flexible membrane seals the annular gap between the cylinder and the steel lining while allowing the cylinder to move vertically. At the start of the first charge, the pressure cylinder remains at its lower travel limit. The reservoir volume is approximately constant, and the air pressure rises as air enters. Once the upward force generated by the pressure difference reaches the lift-off threshold, the cylinder and gravity blocks rise together, increasing the reservoir volume.

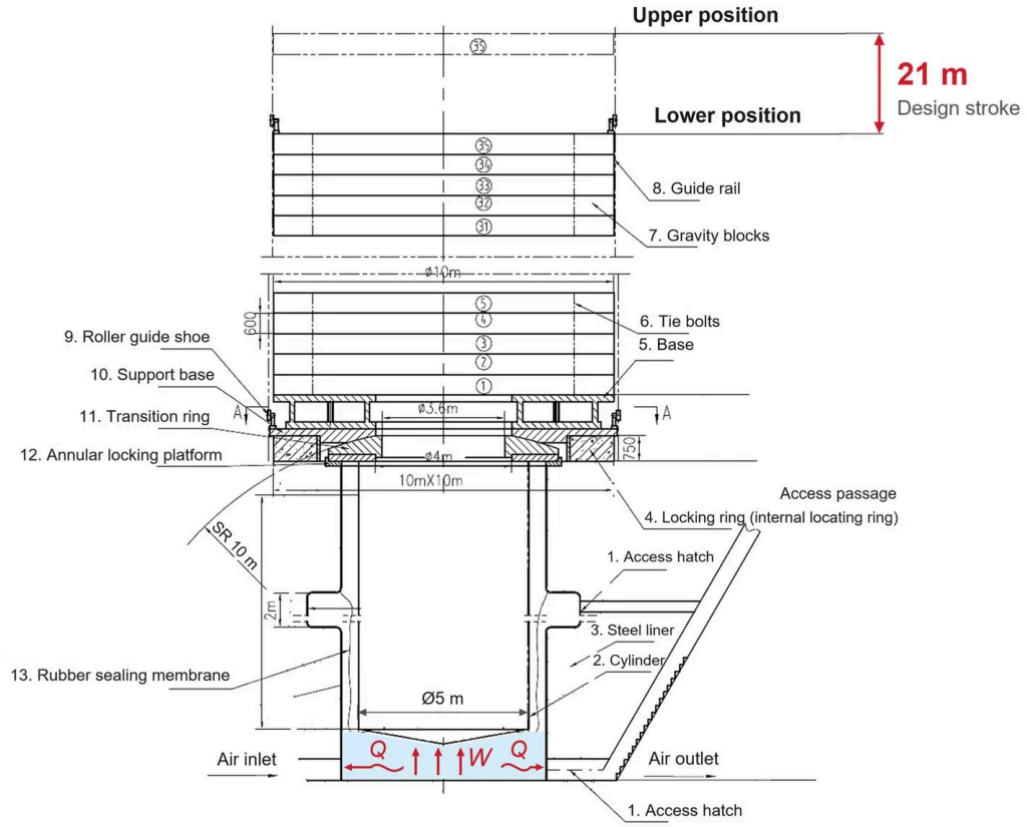


Figure 2. Full-scale G-CAES air reservoir showing the 21 m design stroke and energy transfer paths during charging. *W* denotes the moving-boundary work done by the air on the pressure cylinder, and *Q* denotes heat transfer between the air and the steel lining.

In Figure 2, W denotes the moving-boundary work done by the air on the pressure cylinder during charging, and Q denotes heat transfer between the air and the steel lining. The direction of Q shown in the figure corresponds to conditions in which the air is warmer than the lining. As the moving assembly travels from the lower to the upper limit, its gravitational potential energy increases by $\Delta E_g = Mg\Delta z$, where *M* is the total moving mass, *g* is the acceleration due to gravity, and *Δz* is the vertical displacement. For a moving mass of 6100 t and a design stroke of 21 m, the gravitational potential energy gain is approximately 1.26 GJ.

3. Numerical Model of G-CAES

3.1. Model Assumptions

A complete G-CAES operating cycle comprises four stages: compression (charging), storage at maximum volume, expansion (discharging), and storage at minimum volume, as illustrated in Figure 3. The interval $0 - t_1$ represents charging, during which the pressure cylinder rises, and m_{in} denotes the mass flow rate of air supplied by the compressor to the reservoir. The interval $t_1 - t_2$ corresponds to storage at the upper position after charging. During $t_2 - t_3$, the pressure cylinder descends and performs work during the expansion stage, with m_{out} denoting the air mass flow rate supplied to the expander. The interval $t_3 - t_4$ represents storage at the lower position after discharge, completing a quasi-isobaric operating cycle.

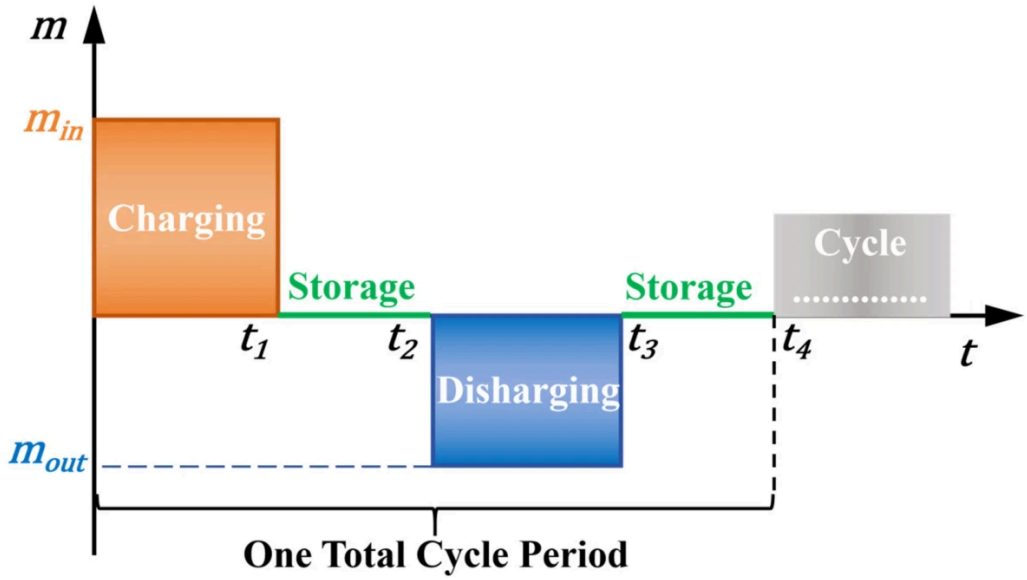


Figure 3. Operating cycle of the G-CAES system. The black vertical dashed line marks the end of one complete operating cycle. The blue horizontal dashed line indicates the discharge mass flow rate, and the white dotted line in the grey "Cycle" region indicates continuation into subsequent cycles.

Initial charging comprises constant-volume pressurization before cylinder lift-off and variable-volume charging after lift-off. Within its effective stroke, the pressure cylinder adjusts the reservoir volume through vertical motion to achieve near-isobaric operation. The actual pressure and cylinder elevation are jointly governed by the gas state, the dynamics of the pressure-bearing assembly, and the stroke constraints.

To investigate transient flow, gas–solid heat transfer, and pressure cylinder motion while retaining the principal geometric features and physical processes, the following assumptions are adopted:

1. At the beginning of the simulation, the air in the reservoir and all solid components considered are in thermal equilibrium at ambient temperature. The temperature fields subsequently evolve continuously across successive cycles.
2. The computational domain primarily includes the air reservoir, gravity blocks, pressure cylinder, and steel lining. Geometric details of auxiliary components, such as guide rails, are neglected. All solid materials are considered isotropic, with constant density, specific heat capacity, and thermal conductivity over the investigated temperature range.
3. The geometric features of the reservoir inlet, outlet, and specified flow passages are retained. The complete external piping network, compressor, and turbine are not explicitly modeled. Their effects are represented through boundary conditions, including inlet and outlet mass flow rates and inlet temperature. Heat exchange between the air and external piping or equipment is not solved separately.
4. The gravity blocks, pressure cylinder, and steel lining are treated as rigid components, and elastic and thermal deformation are neglected. The pressure cylinder and gravity blocks move as a single assembly, with only vertical translation considered.
5. Gas leakage through the sealing system and solid boundaries is neglected. Mass exchange between the reservoir and its surroundings occurs exclusively through the prescribed inlet and outlet.
6. The flexible sealing membrane is not explicitly represented geometrically, and the effect of its local deformation on the effective storage volume is neglected. Its sealing function is represented by impermeable walls with a no-slip condition. At mov-

ing walls, the fluid velocity equals the wall velocity.

7. This study focuses on how changes in storage volume induced by the vertical motion of the pressure cylinder affect the temperature evolution within the air storage chamber. To account for axial friction in the equation of motion, the friction force during ascent and descent is represented by an equivalent force of constant magnitude acting opposite to the direction of cylinder motion. The model neglects transitions between static and sliding friction at the onset and cessation of motion. The magnitude of the equivalent friction force is given in Table 1.

Table 1. Air reservoir parameters.

Parameter	Value
Air reservoir radius (m)	3
Initial air reservoir height (m)	1
Lower limit of air reservoir height (m)	1
Upper limit of air reservoir height (m)	21
Inlet and outlet radii (m)	0.5
Total mass of the pressure cylinder and gravity blocks (t)	6100
Sliding friction force magnitude (kN)	6000
Steel lining thickness (m)	0.5
Ambient temperature (K)	293.15
Prescribed temperature at the outer surface of the steel lining (K)	293.15
Initial air reservoir pressure (MPa)	0.1
Thermal conductivity of the steel lining (W/(m·K))	45
Steel lining density (kg/m^3)	7850
Steel lining specific heat capacity (J/(kg·K))	500

3.2. Governing Equations and Heat Transfer Analysis

3.2.1. Fluid Flow and Turbulence Model

During charging and discharging under gravitational loading, the high-pressure air in the reservoir exhibits compressible, unsteady turbulent flow. The pressure cylinder also causes large, continuous deformation of the computational domain. An arbitrary Lagrangian–Eulerian (ALE) moving mesh formulation is used to update the gas domain as the pressure cylinder moves. The governing equations are solved using the finite element method. The continuity and momentum equations are given below in conservative form in spatial coordinates.

$$\frac{\partial \rho}{\partial t} + \nabla \cdot (\rho u) = 0, \tag{1}$$

$$\frac{\partial (\rho u)}{\partial t} + \nabla \cdot (\rho u u) = -\nabla p + \nabla \cdot \left[(\mu + \mu_T) \left(\nabla u + (\nabla u)^T \right) - \frac{2}{3} (\mu + \mu_T) (\nabla \cdot u) I - \frac{2}{3} \rho k I \right] + \rho g, \tag{2}$$

Here, ρ , u, and p denote the air density, velocity vector, and static pressure in the reservoir, respectively. I is the second-order identity tensor, k is the turbulent kinetic en-

ergy, and μ and μ_T are the molecular dynamic viscosity and turbulent viscosity, respectively. The vector g denotes the gravitational acceleration directed vertically downward. The gravity term accounts for buoyancy arising from spatial variations in air density and allows the model to represent natural convection driven by temperature differences between the air and the steel liner during the holding stages.

During charging and discharging, velocity gradients near the inlet and outlet promote turbulent mixing and influence heat transport within the reservoir. Because this study focuses on the evolution of the mean air temperature over the operating cycle, the standard two-equation $k-\varepsilon$ model is used to represent turbulent momentum transport in the gas domain. The same closure has been used to simulate charging and discharging flows in a fixed-volume compressed air energy storage reservoir [17].

$$\frac{\partial(\rho k)}{\partial t}+\nabla\cdot(\rho u k)=\nabla\cdot\left[\left(\mu+\frac{\mu_T}{\sigma_k}\right)\nabla k\right]+P_k-\rho\varepsilon, \tag{3}$$

$$\frac{\partial(\rho\varepsilon)}{\partial t}+\nabla\cdot(\rho u\varepsilon)=\nabla\cdot\left[\left(\mu+\frac{\mu_T}{\sigma_\varepsilon}\right)\nabla\varepsilon\right]+C_{\varepsilon1}\frac{\varepsilon}{k}P_k-C_{\varepsilon2}\rho\frac{\varepsilon^2}{k}, \tag{4}$$

Here, ε is the turbulent dissipation rate; σ_k and σ_ε are the effective turbulent Prandtl numbers for turbulent kinetic energy and dissipation rate, respectively; $C_{\varepsilon1}$ and $C_{\varepsilon2}$ are empirical constants of the standard turbulence model; and P_k is the production of turbulent kinetic energy due to mean velocity gradients. The turbulent viscosity is calculated as ($\mu_T = \rho C_\mu k^2/\varepsilon$). The standard model constants are (C_μ = 0.09), ($C_{\varepsilon1}$ = 1.44), ($C_{\varepsilon2}$ = 1.92), (σ_k = 1.0), and (σ_ε = 1.3).

Gas-phase buoyancy is accounted for in the mean momentum equation. The turbulence transport equations retain shear production and omit explicit buoyancy source terms. This approximation may affect the simulated local heat transfer rates during the holding stages when buoyancy substantially modifies turbulent mixing. In recirculation and near-wall regions, the simulated temperature gradients and wall heat fluxes may also be sensitive to the isotropic eddy-viscosity assumption and the near-wall treatment.

3.2.2. Energy and Heat Transfer Models

In addition to convective heat transfer, the compressibility of the high-pressure air causes conversion between mechanical energy and internal energy as fluid elements expand and contract, producing transient compression heating and expansion cooling. The gas-phase energy equation includes a pressure-work term to account for compression heating and expansion cooling. Temperature variations in the reservoir are jointly governed by energy transport associated with charging and discharging, pressure work, and gas–solid heat transfer. Considering unsteady compressible flow and turbulent thermal diffusion, while neglecting radiative heat transfer and other volumetric heat sources, the fluid temperature equation is written as:

$$\rho C_p(\partial T/\partial t+u\cdot\nabla T)=\nabla\cdot\left(\lambda_{eff}\nabla T\right)+\alpha_p T\left(\partial p_{abs}/\partial t+u\cdot\nabla p_abs\right) \tag{5}$$

Here, ρ is the gas density, C_p is the specific heat capacity at constant pressure, u is

the gas velocity vector, and p_{abs} is the absolute pressure. The isobaric thermal expansion coefficient is defined as $\alpha_p = -\frac{1}{\rho}\left(\frac{\partial \rho}{\partial T}\right)_{p_{abs}}$, where the density derivative is evaluated at constant absolute pressure. The effective thermal conductivity λ_{eff} is the sum of the molecular thermal conductivity λ_f and the turbulent thermal conductivity λ_T. The turbulent contribution is calculated as $\lambda_T = \frac{\mu_T C_p}{Pr_T}$, where μ_T is the turbulent viscosity defined in Section 3.2.1 and Pr_T is the turbulent Prandtl number.

Within the solid components surrounding the reservoir, including the steel lining and pressure cylinder, energy transport is governed solely by transient heat conduction because macroscopic mass flow and pressure work are absent. The energy conservation equation for the solid domain is:

$$\rho_s C_{p,s} \frac{\partial T_s}{\partial t} = \nabla \cdot (\lambda_s \nabla T_s), \quad (6)$$

Here, ρ_s, $C_{p,s}$ and λ_s are the density, specific heat capacity, and thermal conductivity of the solid material, respectively, and T_s is the transient temperature field within the solid.

During charging and discharging with a variable reservoir volume, transient heat transfer across the gas–solid interface couples the evolution of the gas temperature and density fields. This coupling affects the rate of volume compensation required to maintain isobaric operation. Conjugate heat transfer between the air and the steel liner is solved using the standard thermal wall function in COMSOL Multiphysics 6.1 to describe near-wall heat transfer on the gas side. With the unit normal n pointing from the steel liner into the gas, the interfacial heat flux density is given by:

$$q''_{s \to f} = -\lambda_s \nabla T_s \cdot n = h_{wf}\left(T_w - T_{f,off}\right), \; h_{wf} = \frac{\rho C_p u_\tau}{T^+}, \quad (7)$$

Here, λ_s and T_s are the thermal conductivity and temperature field of the steel liner, respectively. T_w is the physical temperature of the inner steel surface, and $T_{f,off}$ is the gas temperature at the near-wall location used by the thermal wall function. The local effective heat transfer coefficient h_{wf} is calculated from the wall function, where u_τ is the friction velocity and T^+ is the dimensionless temperature. The normal conductive heat flux on the solid side balances the heat flux evaluated by the wall function on the gas side.

3.2.3. Governing Equations

The core operating mechanism of G-CAES involves conversion between the gravitational potential energy of the gravity piston and the pressure energy of the high-pressure air. During operation, the displacement and velocity of the upper reservoir boundary are governed by the instantaneous motion of the gravity piston.

$$m_{block}\frac{d^2H}{dt^2} + F_0 sgn\left(\frac{dH}{dt}\right) = \left(\bar{p}_b - p_{std}\right)A_{eff} - m_{block}g_{const}, \quad (8)$$

Here, H is the vertical position of the pressure cylinder, m_{block} is the combined mass

of the pressure cylinder and gravity blocks, and $\bar{p}_b$ is the area-averaged absolute gas pressure on the pressure-bearing face. The quantities p_{std}, A_{eff}, and g_{const} denote the ambient atmospheric pressure, the effective pressure-bearing area, and the gravitational acceleration, respectively.

Friction has been included in the vertical force balance of the moving assembly in a related G-CAES system [25]. To simplify the calculation, the sliding friction is represented, in accordance with Assumption 7 in Section 3.1, by a force of constant magnitude F_0 acting opposite to the direction of cylinder motion. This representation follows the Coulomb friction formulation used for pneumatic actuators [26]. Ka'ka et al. approximated friction as 10% of the theoretical piston thrust in their pneumatic-actuator calculations [27]. This literature estimate was used as an engineering analogy to select a nominal resistance scale. In the present model, the gravitational load of the moving assembly was taken as the reference axial-force scale, and F_0 was prescribed as approximately $0.10 m_{block} g_{const}$. For a total moving mass of 6100 t, this corresponds to approximately 6000 kN. This value represents a nominal equivalent axial resistance for the present model; device-specific calibration and assessment of its influence on the pressure and temperature responses remain subjects for future work. The value of F_0 used in the prototype simulation is listed in Table 1.

During charging and discharging, the reservoir behaves as an open thermodynamic system with variable mass and volume. Its transient pressure evolution is directly affected by changes in the mass of the working fluid. In engineering applications, compressor and turbine capacities and operating conditions are generally specified in terms of gas mass flow rates rather than molar flow rates. Accordingly, the transient gas mass balance is formulated from mass conservation as:

$$\frac{dm}{dt} = \dot{m}_{in} \ wv_1(t) + \dot{m}_{out} \ wv_2(t), \tag{9}$$

Here, m is the instantaneous air mass in the reservoir, and $\dot{m}_{in}$ and $\dot{m}_{out}$ are the prescribed positive magnitudes of the inlet and outlet mass flow rates, respectively. The dimensionless rectangular waveforms $wv_1(t)$ and $wv_2(t)$ represent the inlet and outlet valve states. During charging, $wv_1 = +1$ and $wv_2 = 0$, so only the inlet valve is open. During discharging, $wv_1 = 0$ and $wv_2 = -1$, so only the outlet valve is open. Both waveforms are zero during the upper- and lower-position holding stages, when both valves are closed. With this sign convention, inflow increases the air mass in the reservoir and outflow decreases it.

The representative absolute pressure in the reservoir is calculated from the instantaneous air mass, representative gas temperature, and gas volume using the following equation of state:

$$p_{res} = \frac{ZmR_g T_{ave}}{V_{gas}(t)} = \frac{ZmR_g T_{ave}}{A_{eff} \cdot H(t)}, \tag{10}$$

Here, Z is the compressibility factor, R_g is the specific gas constant for air, T_{ave} is the mean reservoir temperature obtained by spatial averaging through the heat transfer interface, and V_{gas} is the instantaneous reservoir volume governed by the gravity block displacement H(t). Here, p_{res} is the representative absolute reservoir pressure obtained from Equation (10), m is the instantaneous air mass, and R_g is the specific gas constant for air. The mean air temperature T_{ave} is calculated by taking the area average of the temperature field over the instantaneous gas domain of the two-dimensional reservoir

model. Air is modeled as an ideal gas in the compressible-flow simulation, so the compressibility factor is set to Z = 1 in Equation (10).

The instantaneous gas volume is given by $V_{gas}(t) = V_0 + A_{eff}[H(t) - H_0]$, where H(t) is the instantaneous reservoir height, H_0 is its initial value, and A_{eff} is the effective cross-sectional area. In the prototype simulation, H_0 = 1 m, giving an initial gas volume of $V_0 = A_{eff}H_0$.

In practical installations, the travel of the gravity blocks may be restricted by shaft depth and structural constraints. An initial reservoir volume must also be retained to allow air admission before charging. A discrete event tracking mechanism is therefore introduced to constrain the displacement of the gravity blocks. Their instantaneous kinematic variables must satisfy the following two sets of implicit event conditions.

(1) Upper travel limit

Let H_{max} denote the maximum design stroke. When the upward displacement residual satisfies $\Delta_{up} = H - H_{max} \geq 0$, an upper stop event is triggered, and the dynamic state variables are reset as follows: Let H_{max} denote the upper travel limit of the pressure cylinder. When the cylinder reaches H_{max} while moving upward, an upper-stop event is triggered. The cylinder position is set to H_{max}, and its vertical velocity is reset to zero.

$$H\left(t^+\right) = H_{\max}, \; v\left(t^+\right) = 0, \tag{11}$$

(2) Lower travel limit

Let H_{min} denote the lower travel limit of the pressure cylinder. When the cylinder reaches H_{min} while moving downward, a lower-stop event is triggered. The cylinder position is set to H_{min}, and its vertical velocity is reset to zero.

$$H\left(t^+\right) = H_{\min}, v\left(t^+\right) = 0, \tag{12}$$

These unilateral contact conditions are physically equivalent to perfectly rigid stops at both ends of the stroke. They prevent the pressure cylinder from moving beyond its prescribed limits, ensuring that the range of reservoir volume variation remains governed by the geometric design parameters of the physical system.

3.3. Computational Domain

A two-dimensional planar computational domain with explicit inlet and outlet flow passages is employed to investigate transient flow, gas–solid heat transfer, and pressure cylinder motion. The domain includes the gas within the reservoir and its inlet and outlet passages, together with the solid domains representing the gravity blocks, pressure cylinder, and steel lining. The pressure cylinder and gravity blocks translate vertically as a single assembly, changing the effective reservoir volume, while the steel lining remains stationary.

The selected vertical section contains the inlet and outlet passages and the moving pressure-cylinder boundary. It provides a common plane for examining how gas flow, gas–solid heat transfer, and cylinder motion interact during charging and discharging. Previous CAES studies have used a planar cross-section to investigate the transient thermal response of a cylindrical cavern [28] and a two-dimensional axisymmetric model to analyze reservoir heat transfer during charging and discharging [17]. In the present study, the planar model is used to assess the overall reservoir thermal response and the flow and temperature distributions within the selected section. Circumferential variations and local three-dimensional jet structures remain limitations of this representation. Table 1 lists the principal prototype dimensions, material properties, initial conditions,

and prescribed outer-wall temperature. Initially, the gas and solid domains are in thermal equilibrium at the ambient temperature of 293.15 K. The geometric features of the inlet, outlet, and connecting passages are retained to capture the unsteady disturbances generated by high-pressure air injection and release and their effects on the internal flow and temperature distributions.

The temperature field within the steel lining is obtained by solving the transient heat conduction equation and is coupled to the gas temperature field through the gas–solid interface. This treatment accounts for interfacial heat exchange, thermal diffusion within the lining, and heat accumulation in the solid during repeated charging and discharging. A prescribed-temperature (Dirichlet) boundary condition of 293.15 K was applied at the outer surface of the steel lining throughout the simulation.

The cylinder displacement calculated from Equation (8) drives the update of the gas-domain geometry through the ALE formulation. The reservoir volume and pressure load are calculated from prototype dimensions using user-defined expressions in COMSOL. The instantaneous gas volume in Equation (10) is given by $V_{gas}(t) = V_0 + A_{eff}[H(t) - H_0]$, where $H(t)$ is the instantaneous reservoir height and H_0 is its initial value. In the prototype simulation, $H_0 = 1$ m, giving an initial gas volume of $V_0 = A_{eff}H_0$. The inlet and outlet mass flow rates follow the valve schedule defined in Equation (9), and the inlet air temperature is specified for each charging condition. Inlet turbulence was specified using a turbulence intensity of I = 5% and a turbulence length scale of $L_T = 0.07D_h$, where D_h is the hydraulic diameter of the inlet passage.

3.4. Model Development, Validation, and Numerical Solution

3.4.1. Mesh and Time-Step Sensitivity Analysis

The gas and solid domains are meshed within the two-dimensional computational domain described above, with local refinement near the inlet, outlet, and gas–solid interfaces. Near-wall resolution was assessed using the dimensionless wall-distance parameter y^+. Its values on the evaluated gas-side wall boundaries ranged from 30 to 100. An unstructured triangular mesh is used for the solid domain, while the gas domain mesh is updated using the ALE method. The minimum element quality of the deforming mesh is monitored during the simulation, with an automatic remeshing threshold of 0.2. When the mesh quality falls below this threshold, the domain is remeshed and the existing solution is mapped onto the new mesh before transient integration resumes. The governing equations are discretized using the finite element method and solved with a fully coupled approach. Nonlinear iterations employ the Newton–Raphson method with a relative convergence tolerance of 1.0×10^{-3}.

The mesh sensitivity assessment covers the first 240 s of initial charging, including constant-volume pressurization before cylinder lift-off and near-isobaric charging after lift-off. The inlet air temperature and mass flow rate are set to 333.15 K and 4.3 kg/s, respectively, and the prescribed initial system temperature is 293.15 K. Cases 1–5 contain 12,544, 18,230, 26,155, 35,412, and 46,180 elements, respectively. The physical parameters, boundary conditions, and time discretization settings are the same for all cases. The quantities compared are the mean reservoir air temperature, the vertical displacement of the pressure cylinder relative to its initial position, and the mean steel-lining temperature. Figure 4a shows that the mean reservoir air temperature reaches a peak at approximately 141 s and then decreases. Figure 4b shows that the cylinder rises rapidly after lift-off and then continues to rise at a lower rate, while the mean steel-lining temperature increases gradually. Taking Case 5 as the reference, the maximum absolute deviations in mean reservoir air temperature were 6.56 K for Case 3 and 1.39 K for Case 4. Normalizing these deviations by the peak temperature rise in Case 5 gave 6.37% and 1.32%, respectively. Between Cases 4 and 5, the maximum absolute difference in relative

cylinder displacement was 0.034 m, and the maximum difference in mean steel-lining temperature was approximately 4% of the peak steel-lining temperature rise in Case 5. All subsequent simulations were performed using Case 4, which contained 35,412 elements.

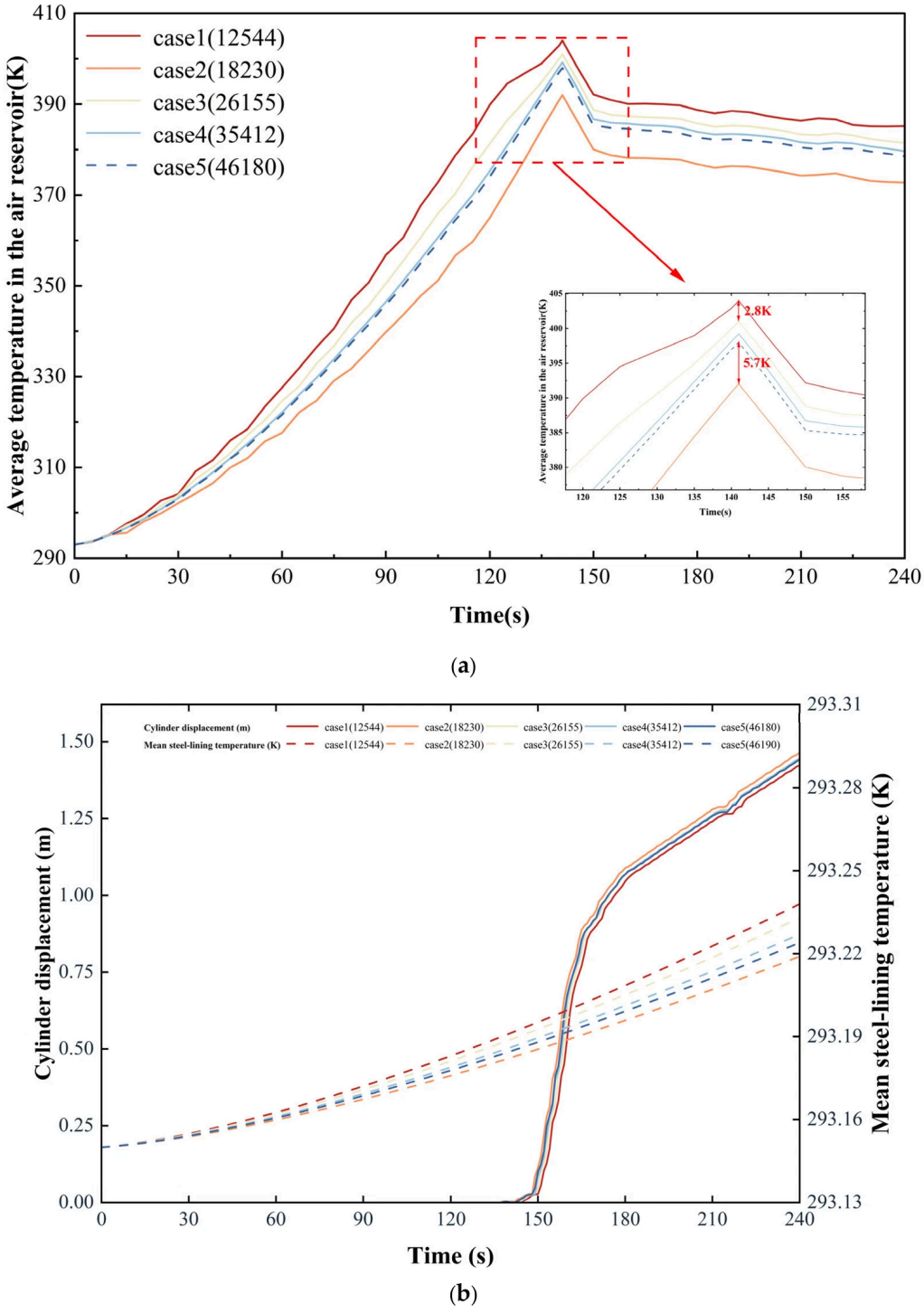


Figure 4. Mesh sensitivity during the first 240 s of initial charging. (**a**) Mean reservoir air temperature. (**b**) Pressure cylinder displacement relative to its initial position (left axis) and mean steel-lining temperature.

The time-step sensitivity assessment was designed for the first 240 s of initial charging on the Case 4 mesh with 35,412 elements. The comparison used the same operating conditions as the mesh sensitivity assessment, with an inlet air temperature of 333.15 K

and an inlet mass flow rate of 4.3 kg/s. Three time-step sizes of 0.1, 0.5, and 1.0 s were considered, with the 0.1 s curve serving as the reference.

As shown in Figure 5, all three mean reservoir air temperature curves reach a peak at approximately 141 s and then decline. The largest deviations from the reference occur at 128 s, before the temperature peak. The maximum absolute deviations are 3.20 K for the 1.0 s curve and 0.31 K for the 0.5 s curve, corresponding to 3.01% and 0.29% of the reference peak temperature rise, respectively. By 150 s, these deviations decrease to 0.85 K and 0.12 K, respectively. Given the close agreement with the 0.1 s reference solution and the smaller number of time steps required, a time step of 0.5 s was adopted for the subsequent transient simulations.

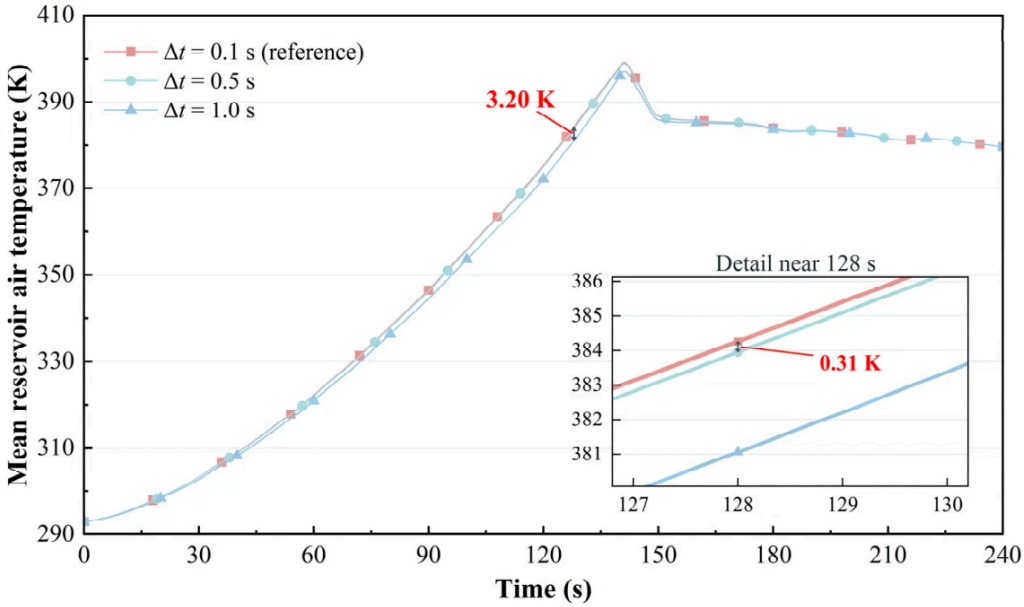


Figure 5. Comparison of the mean reservoir air temperature for three time-step sizes during the first 240 s of initial charging.

3.4.2. Experimental Validation

The numerical model was evaluated against measurements of the transient air temperature in the reservoir of the 1:10-scale experimental rig shown in Figure 6. Air was used as the working fluid. Because gravitational and inertial forces govern the ascent and descent of the pressure cylinder, the durations of the operating stages were determined using the Froude time-scale ratio $\lambda_t = \sqrt{(0.1)}$. Charging and discharging each lasted 18.97 min, and the holding periods at the upper and lower cylinder positions each lasted 9.49 min. The total cycle duration was 56.92 min.



Figure 6. The 1:10-scale G-CAES experimental platform: (**a**) overall setup; (**b**) air storage chamber; (**c**) flexible sealing membrane; (**d**) gravity blocks; (**e**) locking platform; (**f**) data acquisition and analysis interface; (**g**) air compressor; and (**h**) generator. The Chinese sign in (a) means "1 MW gravity compressed air energy storage system model".

A single temperature sensor was installed at the bottom of the reservoir to limit the number of penetrations through the pressure-bearing liner and preserve its airtightness and structural integrity. The sensor had a measurement accuracy of ±0.1 K, and the data were acquired at 20 Hz. Five independent repeat tests were conducted on the same day under the same nominal operating conditions to reduce the influence of random measurement errors. The measured temperature history shown in Figure 7a is the arithmetic mean of the five test records. As the inlet air temperature varied slightly with ambient conditions throughout the day, the mean inlet temperature measured across the five tests, approximately 293 K, was prescribed at the simulation inlet. The numerical model reproduced the geometry and operating boundary conditions of the scaled rig, and the calculated temperature was extracted at the location corresponding to the physical sensor. The start of charging was taken as the common time origin, and the numerical results were linearly interpolated to the experimental sampling times for pointwise comparison.

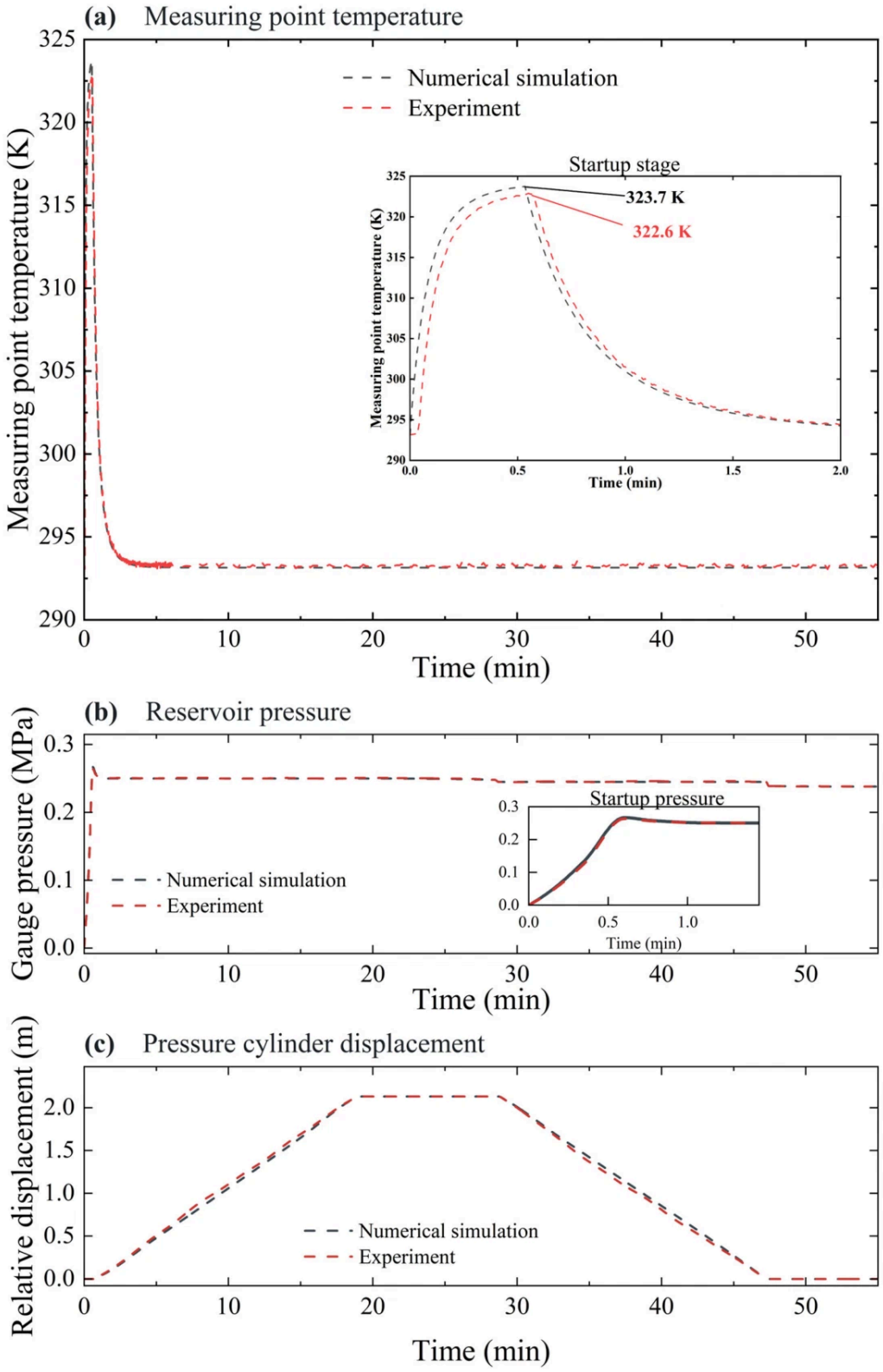


Figure 7. Comparison of numerical simulations and experimental measurements during the first 55 min of the 1:10-scale G-CAES operating cycle. (**a**) Air temperature at the reservoir bottom measurement point. (**b**) Reservoir gauge pressure. (**c**) Vertical displacement of the pressure cylinder relative to its initial position.

Figure 7a compares the simulated and measured air temperatures over the first 55 min of the cycle. The simulated temperature peaked at 323.7 K at 0.53 min, while the measured temperature peaked at 322.6 K at 0.55 min. The absolute difference between

the peak temperatures was 1.1 K. Over the complete cycle, the root-mean-square error (RMSE) was 1.03 K. The RMSE and maximum absolute deviation were 1.16 K and 10.8 K during charging and 0.15 K and 0.4 K during discharging. The maximum absolute deviation over the cycle occurred approximately 2.5 s after the start of charging, when the air temperature was rising rapidly. Heat conduction between the temperature probe, its mount, and the external liner structure may have contributed to this discrepancy. During rapid heating, conduction through the mount and the thermal inertia of the probe may together delay the probe response and affect the transient readings. Dynamic calibration of the probe and synchronized measurements at multiple locations are needed to quantify the contribution of this effect to the initial discrepancy. The overall RMSE characterizes agreement over the full comparison interval, whereas the maximum deviation of 10.8 K identifies a localized discrepancy during the initial rapid temperature rise. Accordingly, the comparison indicates that the model reproduces the overall temperature evolution and peak magnitude at the measurement location under the tested conditions, while indicating a limitation in reproducing the earliest startup transient.

Figure 7b,c compare the simulated and measured reservoir gauge pressure and pressure cylinder displacement under the same operating conditions of the scaled test rig. At the start of charging, the pressure cylinder remains at its initial position while the reservoir undergoes constant-volume pressurization. At approximately 0.60 min, the reservoir pressure reaches the lift-off threshold and the cylinder begins to rise. During subsequent charging, the gauge pressure stabilizes near 0.25 MPa. The cylinder displacement reaches approximately 2.1 m at the end of charging and remains nearly constant during the upper-position holding period. During discharging, the cylinder descends and returns to its initial position. The reservoir gauge pressure is approximately 0.24 MPa during the lower-position holding period. The maximum absolute difference between the simulated and measured pressure histories is approximately 0.01 MPa and occurs during the initial constant-volume pressurization stage. The maximum absolute difference between the simulated and measured cylinder displacements is approximately 0.064 m.

The comparison with measurements indicates that the numerical model reproduces the overall temperature evolution and peak at the reservoir bottom under the tested scale-model conditions, with a larger local discrepancy during the initial rapid heating stage. Froude scaling provides the time conversion for the overall mechanical motion. The Reynolds number, the characteristic time scales of heat conduction within the steel liner and convective heat transfer at the gas–solid interface, and the gas-to-solid thermal inertia ratio impose additional similarity requirements that must be assessed separately when scaling up to the full-size prototype. The experimental comparisons assess the reservoir pressure, cylinder displacement, and local air temperature at the reservoir bottom under the tested scale-model conditions. Validation of the spatial temperature distribution requires additional temperature measurements at representative locations.

4. Results and Discussion

This section examines the transient thermal response of the air reservoir in a G-CAES system during initial charging and repeated operation. During initial charging, the pressure cylinder remains stationary before lift-off, and the reservoir undergoes constant-volume pressurization. After lift-off, the reservoir volume increases as the cylinder rises, and the system enters a near-isobaric variable-volume charging regime following a brief transition. Before lift-off, the gas energy balance is governed by inlet enthalpy input and gas–solid heat transfer. Once the cylinder begins to rise, the gas also performs work on the moving boundary. Sections 4.1 and 4.2 examine how the inlet air temperature and inlet mass flow rate, respectively, affect the startup temperature peak and its timing.

Section 4.3 analyzes the pressure and cylinder displacement during the first operating cycle and examines the evolution of the gas and steel-lining temperatures over successive cycles.

4.1. Inlet Temperature

To evaluate the effect of inlet air temperature on the thermal response of the reservoir during initial charging, five inlet temperatures are considered: 293.15, 303.15, 313.15, 323.15, and 333.15 K. Air is supplied at a constant mass flow rate of 4.3 kg/s throughout the 60 min charging period. Figure 8 shows the evolution of the mean reservoir gas temperature during constant-volume pressurization before cylinder lift-off and near-isobaric variable-volume charging after lift-off.

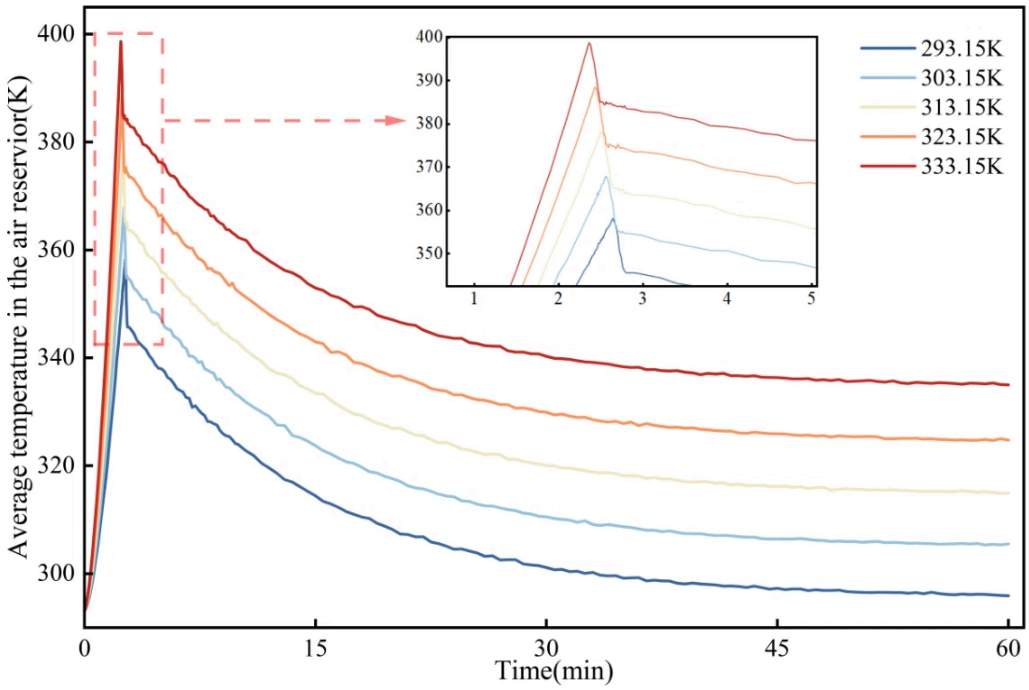


Figure 8. Mean reservoir temperature at different inlet temperatures.

As shown in Figure 8, increasing the inlet air temperature from 293.15 to 333.15 K at a fixed mass flow rate of 4.3 kg/s raised the peak mean reservoir gas temperature from 358.27 to 398.68 K, an increase of 40.41 K. The peak occurred at 2.36 min instead of 2.64 min, approximately 17 s earlier. Using a representative constant-pressure specific heat of 1.005 kJ/(kg·K) for air over this temperature range, the 40 K increase in inlet temperature corresponds to an increase of approximately 40.2 kJ/kg in inlet specific enthalpy and 173 kW in inlet enthalpy flow rate. Before cylinder lift-off, the reservoir volume remains constant, and the higher inlet enthalpy flow rate increases the rate of energy input to the gas. At a given gas mass and reservoir volume, a higher gas temperature also corresponds to a higher reservoir pressure, favoring earlier attainment of the pressure required for lift-off. These effects are consistent with the higher and earlier startup temperature peak observed at the higher inlet air temperature. At an inlet air temperature of 333.15 K, the mean reservoir gas temperature dropped from its peak of 398.68 K to 384.93 K within approximately 9 s. The pressure and cylinder displacement histories for the same case in Section 4.3 show that this rapid decrease coincided with the onset of cylinder lift-off and the increase in reservoir volume. As the gas expands, it performs work on the moving boundary, transferring energy out of the gas. During the subsequent near-isobaric variable-volume charging stage, the mean reservoir gas temperature

is governed by the balance among continued inlet enthalpy input, work done on the moving boundary, and convective heat transfer at the gas–solid interface. The mean reservoir gas temperature then decreased gradually to approximately 335 K at the end of charging.

4.2. Inlet Mass Flow Rate

To examine the effect of inlet mass flow rate on the transient thermal response of the reservoir, five mass flow rates are compared at a constant inlet temperature of 333.15 K: 12.90, 6.45, 4.30, 2.87, and 2.15 kg/s. Figure 9 presents the mean reservoir temperature during the first 30 min after startup for each case.

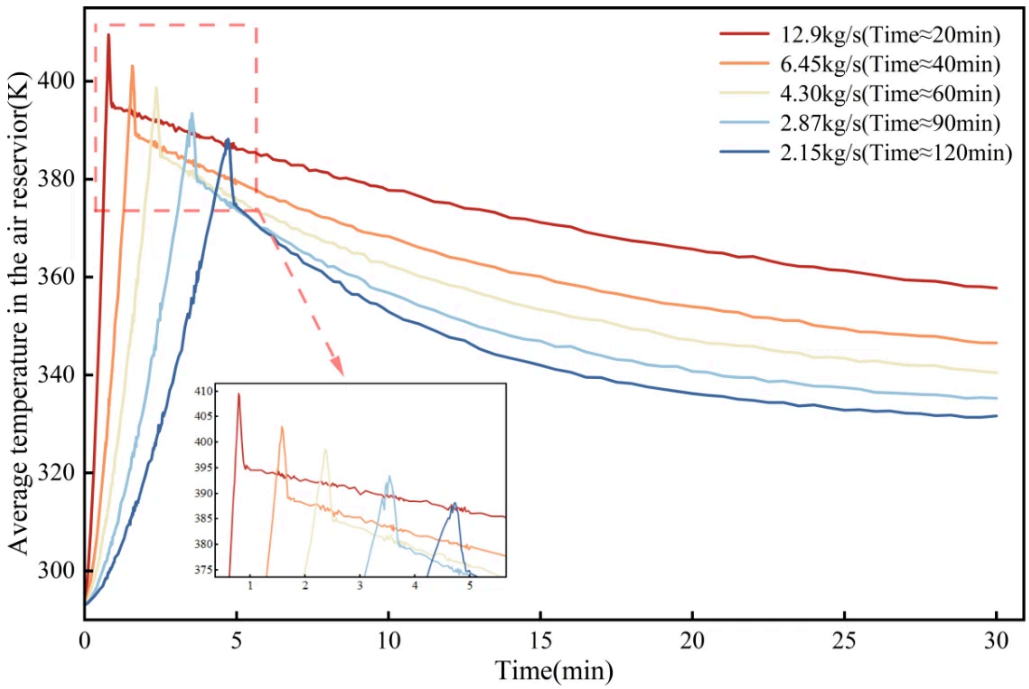


Figure 9. Mean reservoir temperature at different inlet mass flow rates.

As shown in Figure 9, increasing the inlet mass flow rate from 2.15 to 12.90 kg/s raised the peak mean reservoir gas temperature from 388.21 to 409.52 K, an increase of 21.31 K, and reduced the time to peak from 4.72 to 0.78 min. Based on the prescribed mass flow rates and the corresponding times to peak, the cumulative masses of air admitted up to the respective peaks were approximately 609 and 604 kg, a difference of less than 1%. Because the inlet specific enthalpy was approximately the same in both cases, the cumulative enthalpy inputs at the respective peaks were similar. The high-flow case delivered this input in approximately one-sixth of the time required by the low-flow case.

The effect of mass flow rate can be interpreted from the energy balance of the gas in the reservoir. Under the ideal-gas and constant-specific-heat approximations, and with kinetic and potential energy effects neglected, the rate of change in the mass-weighted mean gas temperature depends on the energy supplied by the incoming air, the heat transferred to the solid, and the work done on the moving boundary. The energy available to raise the gas temperature per unit mass of incoming air is the inlet specific enthalpy minus the specific internal energy associated with the added mass at the current reservoir gas temperature. Taking 380 K as a common reference temperature and using specific heats of approximately 1.005 kJ/(kg·K) at constant pressure and 0.718 kJ/(kg·K) at constant volume, this difference is approximately 62 kJ/kg. At this reference state, the es-

timated rate at which the incoming air supplies energy for gas heating is approximately 133 kW at 2.15 kg/s and 800 kW at 12.90 kg/s. The heating term is therefore six times as large in the high-flow case.

Before cylinder lift-off, the reservoir volume is fixed and the gas does no work on the cylinder. For the same cumulative mass inflow during this stage, a higher flow rate allows less time for heat transfer from the gas to the steel lining. If the increase in interfacial heat transfer rate is insufficient to offset the shorter charging time, less heat is transferred to the lining per unit mass of air admitted. The gas then retains more of the inlet energy at the same accumulated mass, and the charging response approaches the adiabatic limit. This mechanism is consistent with the faster temperature rise and higher startup peak in the high-flow case. After lift-off, expansion of the gas against the moving cylinder introduces an additional energy output. When the combined rates of heat loss and boundary work exceed the rate at which the incoming air supplies energy for gas heating, the mean gas temperature decreases. The temperature evolution around the peak thus reflects the changing balance among inlet energy supply, gas–solid heat transfer, and moving-boundary work.

4.3. Analysis of the First and Subsequent Cycles

All reservoir pressures reported in this section are expressed as absolute pressures. For the first operating cycle, the inlet temperature is set to 333.15 K and the charging mass flow rate to 4.3 kg/s. Charging lasts 1 h, followed by 30 min of near-isobaric storage at the upper position. Air is subsequently discharged at 3.85 kg/s for 1 h until the pressure cylinder returns to the reference elevation of 1 m, followed by 30 min of near-isobaric storage at the lower position. The evolution of mean gas temperature, pressure, and cylinder displacement is presented in Figure 10. Figure 11 provides an enlarged view of the initial charging stage, and Figure 12 shows the reservoir temperature distributions. The energy conversion mechanisms during charging and discharging are examined through the response of these key operating variables during the first cycle.

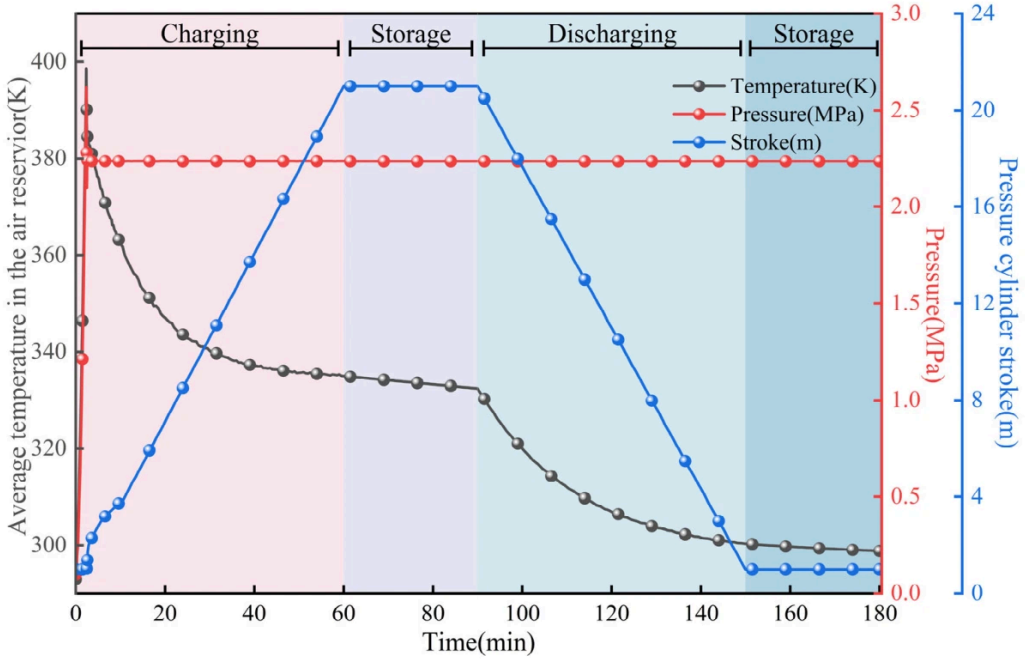


Figure 10. Time evolution of mean reservoir temperature, pressure, and pressure cylinder displacement during the first cycle.

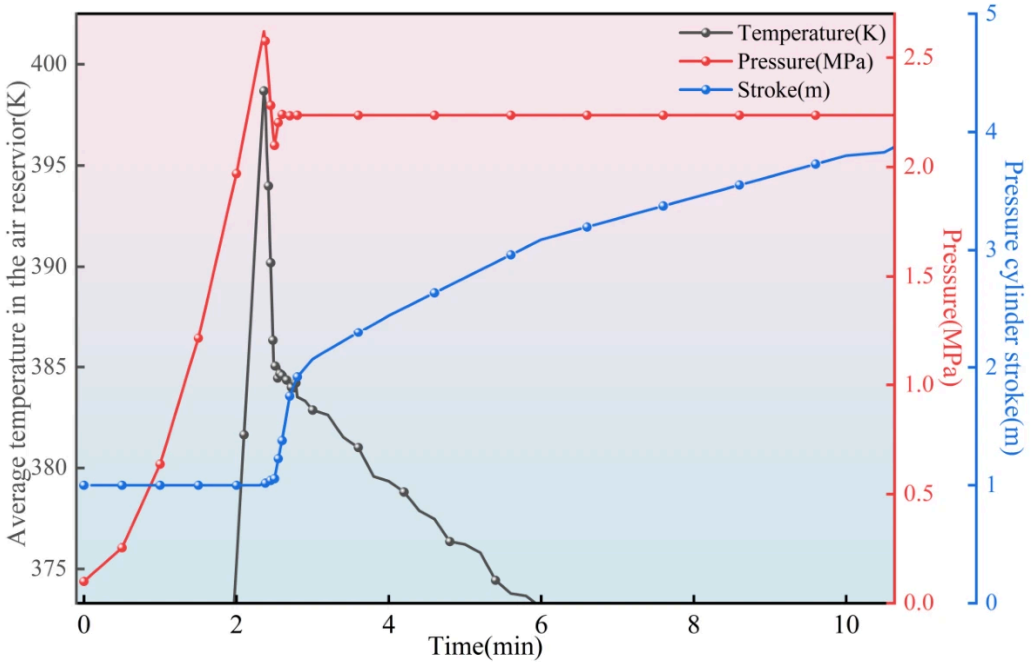


Figure 11. Enlarged view of the initial charging stage during the first cycle.

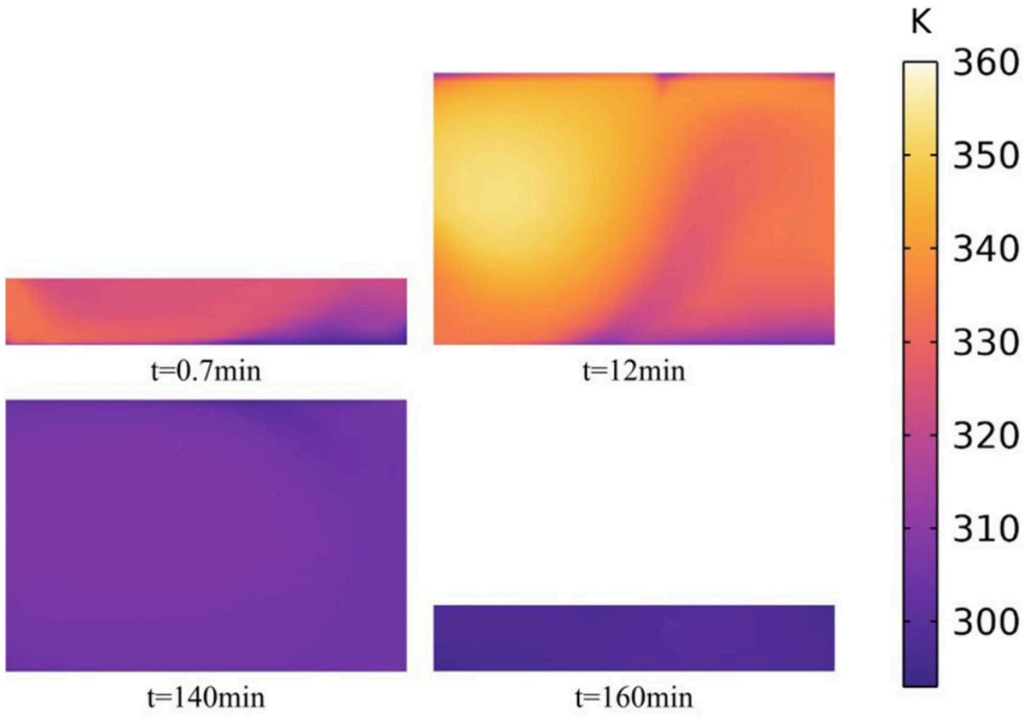


Figure 12. Air temperature distributions in the reservoir at 0.7, 12, 140, and 160 min of the first operating cycle.

During approximately the first 2.3 min of charging, the pressure cylinder remains at its initial elevation of 1.0 m, and the reservoir undergoes approximately constant-volume pressurization. Continuous air injection increases the gas mass, while inlet enthalpy input supplies energy, causing pressure and mean temperature to rise rapidly. As shown in Figure 11, the pressure reaches 2.62 MPa at approximately 2.36 min, and the mean temperature reaches a peak of 398.68 K. Because the volume changes little during this stage, the accumulation of mass and energy associated with air injection is primarily reflected in increasing pressure and temperature.

Once the cylinder lift-off condition is reached, the pressure cylinder begins to move and the reservoir volume increases rapidly. The gas performs work on the moving boundary, causing brief decreases in both pressure and mean temperature. At approximately 2.4 min, the reservoir pressure briefly fell to 2.12 MPa, a decrease of 0.50 MPa, or about 19% of the peak pressure. During the same transition, the mean gas temperature fell from 398.68 to 384.93 K within approximately 0.15 min, a decrease of 13.75 K. Air continued to enter the reservoir while the gas did work on the moving boundary and exchanged heat with the steel lining. These changes reflect the transient coupling between the gas state and cylinder motion during startup. Rapid volume expansion and the associated boundary work play an important role in the temperature decline following the peak.

During subsequent charging, from approximately 2.5 to 60 min, the reservoir pressure remains near 2.24 MPa, and the system enters near-isobaric operation with a variable volume. The pressure cylinder continues to rise and reaches a maximum elevation of 21.0 m at the end of charging, corresponding to an effective stroke of 20.0 m. By adjusting the reservoir volume, cylinder motion compensates for the gas mass added during charging and maintains approximately stable pressure within the effective stroke. The mean reservoir temperature continues to decrease, reaching approximately 335 K at 60 min, consistent with the corresponding case in Section 4.1. Gas temperature evolution is jointly governed by inlet enthalpy input, moving boundary work, and gas–solid heat transfer. Cylinder motion also changes the reservoir geometry, gas–solid contact area, and internal flow conditions, causing the heat transfer process to evolve throughout operation. The temperature contour at 12 min in Figure 12 shows that relatively hot regions and near-wall temperature gradients remain within the reservoir. Thus, the local temperature field remains nonuniform while the mean temperature decreases. Transport of incoming air, internal gas mixing, and gas–solid heat transfer jointly determine this spatial distribution.

After charging, the system enters the upper-position storage stage from 60 to 90 min. Air injection and inlet enthalpy input cease, while the temperature difference between the gas and steel lining continues to drive interfacial heat exchange. Under the boundary constraints applied during this stage, the mean reservoir temperature decreases slowly to 332.47 K at 90 min. The temperature changes more gradually than during startup and early charging, reflecting continued heat exchange between the gas and solid boundaries after air injection stops.

During discharge, from 90 to 150 min, air leaves through the outlet, and the pressure cylinder gradually descends under the gravitational load. The reservoir volume decreases accordingly, while pressure remains approximately stable within the effective stroke. Discharge changes the gas mass and energy in the reservoir, and the temperature response is jointly affected by boundary work associated with cylinder descent and gas–solid heat transfer. The simulations show that the mean temperature decreases more rapidly during discharge than during upper-position storage, reaching 300.31 K at 150 min as the cylinder returns to its initial elevation of 1.0 m. The temperature contour at 140 min in Figure 12 shows a substantially lower overall temperature, less pronounced hot regions than during charging, and a more uniform temperature distribution.

During lower-position storage, from 150 to 180 min, the outlet valve is closed and the mean reservoir temperature continues to decrease slowly. The temperature contour at 160 min in Figure 12 shows smaller macroscopic temperature differences than during charging. By the end of the lower-position dwell at 180 min, the mean reservoir gas temperature had decreased to 298.82 K, which was 5.67 K above its initial value of 293.15 K. The gas and steel-lining temperature fields at the end of the first cycle provided the initial thermal state for the next cycle.

The numerical model described in Section 3 was used to simulate 50 consecutive operating cycles, with the computed gas and solid states at the end of each cycle retained as the initial conditions for the next cycle. Each cycle lasted 3 h, giving a total simulated duration of 150 h. Figure 13 presents the resulting time histories of the mean reservoir air temperature and mean steel-lining temperature. Following the initial startup cycle, the charging peak of the mean air temperature increased from 324.50 K in cycle 2 to 332.60 K in cycle 9. It subsequently decreased to 331.85 K in cycle 10 and gradually approached 331.73 K during the later cycles.

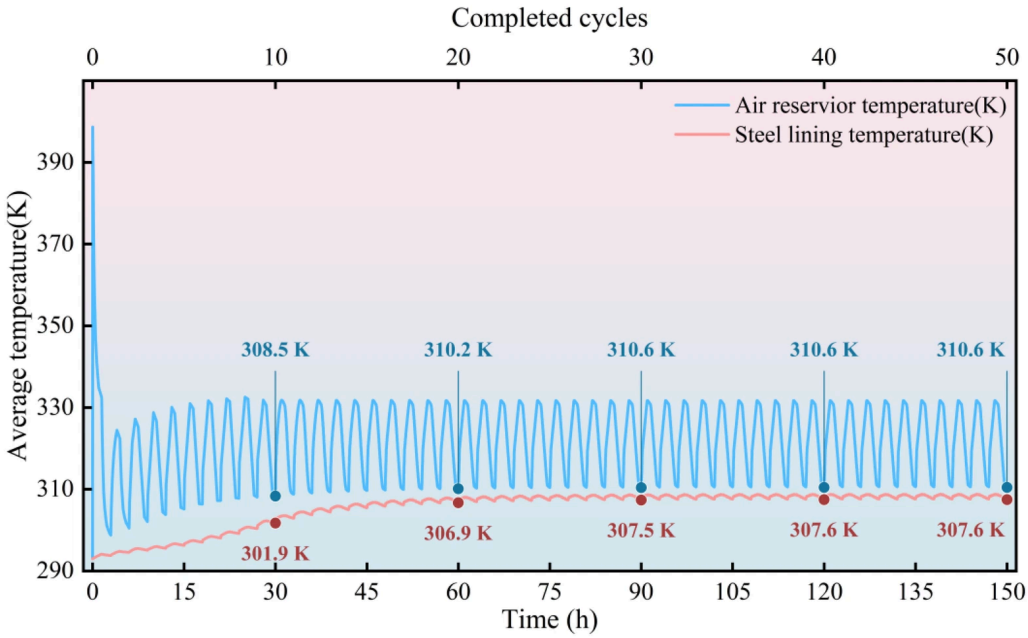


Figure 13. Mean reservoir air and steel-lining temperatures over 50 operating cycles.

The end of the lower-position dwell period was selected as the common operating phase for comparing end-of-cycle temperatures. At the ends of cycles 10, 20, 30, 40, and 50, the mean reservoir air temperatures were 308.50, 310.24, 310.55, 310.61, and 310.62 K, respectively. The corresponding mean steel-lining temperatures were 301.90, 306.86, 307.54, 307.63, and 307.64 K. Both end-of-cycle temperatures increased over successive cycles, with substantially smaller increments during the later cycles.

Between cycles 10 and 20, the end-of-cycle mean air and steel-lining temperatures increased by 1.74 and 4.96 K, respectively. Between cycles 20 and 50, the corresponding increases decreased to 0.38 and 0.78 K. The average rise in the end-of-cycle steel-lining temperature therefore decreased from approximately 0.50 K per cycle over cycles 10–20 to approximately 0.03 K per cycle over cycles 20–50. During the final ten cycles, from cycle 40 to cycle 50, both end-of-cycle temperatures increased by approximately 0.01 K.

The absolute differences in end-of-cycle temperatures between cycles 19 and 20 were 0.07 K for the mean reservoir air temperature and 0.17 K for the mean steel-lining temperature. Between cycles 29 and 30, these differences decreased to 0.01 and 0.03 K, respectively. At the precision of 0.01 K, cycles 49 and 50 had identical reported end-of-cycle temperatures. In cycle 50, the charging peak of the mean reservoir air temperature was 331.73 K, exceeding its end-of-cycle value of 310.62 K by 21.11 K. The progressively smaller changes in end-of-cycle temperatures, together with the stabilization of the charging temperature peak, indicate diminishing cycle-to-cycle thermal drift and are consistent with an approach toward a repeatable cyclic thermal response under the investigated operating and thermal boundary conditions.

5. Conclusions

A two-dimensional transient numerical model coupling compressible air flow, conjugate heat transfer between the air and the steel lining, and pressure cylinder motion was developed to investigate the thermal response of an air reservoir in a G-CAES system. The study examined initial charging, the effects of inlet conditions, and the thermal response over successive operating cycles. The main conclusions are as follows:

(1) Initial charging comprises a constant-volume pressurization stage before cylinder lift-off and a near-isobaric, variable-volume stage after lift-off. Before lift-off, continuous inflow increases the mass and internal energy of the reservoir air, causing its mean temperature to rise rapidly. After lift-off, the reservoir volume increases and the air does work on the moving boundary. The mean air temperature then evolves in response to inlet enthalpy flow, moving-boundary work, and heat transfer between the air and the steel lining. At an inlet air temperature of 333.15 K and an inlet mass flow rate of 4.30 kg/s, the mean reservoir air temperature peaked at 398.68 K at 2.36 min and fell to 384.93 K within approximately 9 s. This rapid decrease coincided with cylinder lift-off and the increase in reservoir volume.

(2) Within the investigated parameter range, increasing either inlet temperature or mass flow rate produces a higher and earlier startup temperature peak. At a mass flow rate of 4.3 kg/s, increasing the inlet temperature from 293.15 to 333.15 K raises the peak temperature from 358.27 to 398.68 K. At an inlet temperature of 333.15 K, increasing the mass flow rate from 2.15 to 12.90 kg/s raises the peak temperature from 388.21 to 409.52 K and advances its occurrence from 4.72 to 0.78 min. These results indicate that inlet parameters should be selected with consideration of their effects on the startup peak temperature and the duration of initial heating.

(3) The numerical simulation of 50 consecutive operating cycles showed progressive warming of the steel lining, accompanied by diminishing changes in the characteristic air temperatures. The mean steel-lining temperatures at the ends of cycles 10, 20, and 50 were 301.90, 306.86, and 307.64 K, respectively. The average increase in the end-of-cycle steel-lining temperature decreased from approximately 0.50 K per cycle over cycles 10–20 to approximately 0.03 K per cycle over cycles 20–50. Between cycles 40 and 50, the end-of-cycle mean air and steel-lining temperatures each increased by approximately 0.01 K. By cycle 50, the end-of-cycle mean air temperature and charging temperature peak were 310.62 and 331.73 K, respectively. These changes indicate diminishing cycle-to-cycle thermal drift, consistent with an approach toward a repeatable cyclic thermal response under the investigated operating conditions and the prescribed outer steel-lining temperature of 293.15 K.

As formulated, the proposed model is intended for use only in the analysis of G-CAES air reservoirs. The conclusions are specific to the reservoir configuration, operating conditions, and thermal boundary conditions investigated in this study. The two-dimensional planar model used the standard k–ε turbulence model and the standard thermal wall function, with the outer surface of the steel lining held at 293.15 K. The steel-lining temperature levels and the approach toward a repeatable cyclic thermal response obtained from the numerical simulations depend on the prescribed outer-surface temperature of 293.15 K. This boundary assumption affects heat rejection from the lining and thermal accumulation during repeated operation. Therefore, the resulting temperature levels and cyclic thermal behavior are specific to the investigated thermal boundary condition, and the effects of alternative external boundary conditions require further investigation. Future work could compare the planar model with an axisymmetric model using equivalent inlet and outlet boundary conditions and a three-dimensional model retaining the actual spatial arrangement of the inlet and outlet. Comparisons under representative operating conditions could quantify the effects of geometric simplification on

the simulated air temperature distribution and gas–solid interfacial heat flux. Comparisons with other turbulence models are left for future work.

Experimental validation was limited to the air temperature history measured at a single point at the bottom of the reservoir in a 1:10-scale test rig. Future experiments could add air temperature sensors at different elevations and, where feasible, at different radial positions to assess the simulated spatial temperature distribution. Additional sensors in the steel lining could help assess its simulated temperature evolution. Sensor placement should preserve the airtightness of the reservoir and the structural integrity of the lining. Repeated tests could quantify run-to-run variability, and dynamic calibration of the temperature probe could help assess the influence of heat conduction through the sensor mount on startup readings. The transient steel-lining temperature field obtained from the coupled model could also serve as a thermal load in subsequent solid mechanics analyses of steel-lining stress and deformation during cyclic operation.

Author Contributions: Conceptualization, Y.H. and W.N.; methodology, Z.S., Y.H. and L.M.; validation, Z.S. and X.W. (Xiaodong Wang); formal analysis, Z.S. and L.M.; investigation, Z.S., X.W. (Xiaodong Wang) and X.W. (Xing'en Wang); resources, X.W. (Xiaodong Wang) and W.N.; data curation, Z.S. and X.W. (Xing'en Wang); writing—original draft preparation, Z.S.; writing—review and editing, Y.H., L.M., X.W. (Xiaodong Wang), W.N. and X.W. (Xing'en Wang); visualization, Z.S.; supervision, Y.H. and W.N.; project administration, W.N. All authors have read and agreed to the published version of the manuscript.

Funding: This research was funded by Jiangsu Provincial Joint Consortium for Core Technology R&D and Industrialization of Gravity Compressed Air Energy Storage (grant no. (2024) LHT 2024009-04 & Rq125001), the National Natural Science Foundation of China (grant no. 52309099), Guizhou Provincial Academician Innovation Team Workstation for New Integrated Energy (grant no. KXJZ [2024]011), Nanjing Hydraulic Research Institute Graduate Thesis Innovation Fund (2026) (grant no. Yy126016) and Jiangsu Provincial Postgraduate Research and Practice Innovation Program (grant no. 26CXJH7515).

Data Availability Statement: The data supporting the findings of this study are not publicly available due to project-related data-sharing restrictions. Requests for access may be directed to the authors and will be considered in accordance with the applicable project requirements.

Conflicts of Interest: Author Xing'en Wang was employed by the company PowerChina Guiyang Engineering Corporation Limited and is also pursuing a part-time doctoral degree at the Nanjing Hydraulic Research Institute. The remaining authors declare that the research was conducted in the absence of any commercial or financial relationships that could be construed as potential conflicts of interest.

Abbreviations

The following abbreviations are used in this manuscript:

G-CAES	Gravity compressed air energy storage
CAES	Compressed air energy storage
HTF	Hot heat transfer fluid

References

1. International Energy Agency. *Renewables 2025: Analysis and Forecasts to 2030*; International Energy Agency: Paris, France, 2025. Available online: https://www.iea.org/reports/renewables-2025 (accessed on 12 November 2026). [Google Scholar]
2. Ribeiro, P.F.; Johnson, B.K.; Crow, M.L.; Arsoy, A.; Liu, Y. Energy storage systems for advanced power applications. *Proc. IEEE* **2001**, *89*, 1744–1756. [Google Scholar] [CrossRef] [PubMed]

3. Budt, M.; Wolf, D.; Span, R.; Yan, J. A review on compressed air energy storage: Basic principles, past milestones and recent developments. *Appl. Energy* **2016**, *170*, 250–268. [Google Scholar] [CrossRef]
4. Geissbühler, L.; Becattini, V.; Zanganeh, G.; Zavattoni, S.; Barbato, M.; Haselbacher, A.; Steinfeld, A. Pilot-scale demonstration of advanced adiabatic compressed air energy storage, Part 1: Plant description and tests with sensible thermal-energy storage. *J. Energy Storage* **2018**, *17*, 129–139. [Google Scholar] [CrossRef]
5. Becattini, V.; Geissbühler, L.; Zanganeh, G.; Haselbacher, A.; Steinfeld, A. Pilot-scale demonstration of advanced adiabatic compressed air energy storage, Part 2: Tests with combined sensible/latent thermal-energy storage. *J. Energy Storage* **2018**, *17*, 140–152. [Google Scholar] [CrossRef]
6. Bouzennada, T.; Abderrahmane, A.; Younis, O.; Oreijah, M.; Guedri, K.; Maatki, C.; Kolsi, L. Numerical simulation of heat transfer and melting process in a NEPCM: Using new fin shape. *Int. Commun. Heat Mass Transf.* **2023**, *143*, 106711. [Google Scholar] [CrossRef]
7. Yang, S.; Zhang, Y.; Gao, Z.; Liu, Z. Isobaric compressed air energy storage system: Water compensating cycle or CO_2 compensating cycle? *Energy* **2024**, *312*, 133682. [Google Scholar] [CrossRef]
8. Giramonti, A.J.; Lessard, R.D.; Blecher, W.A.; Smith, E.B. Conceptual design of compressed air energy storage electric power systems. *Appl. Energy* **1978**, *4*, 231–249. [Google Scholar] [CrossRef]
9. Pimm, A.J.; Garvey, S.D.; de Jong, M. Design and testing of Energy Bags for underwater compressed air energy storage. *Energy* **2014**, *66*, 496–508. [Google Scholar] [CrossRef]
10. Cheung, B.C.; Carriveau, R.; Ting, D.S.-K. Parameters affecting scalable underwater compressed air energy storage. *Appl. Energy* **2014**, *134*, 239–247. [Google Scholar] [CrossRef]
11. Pimm, A.J.; Garvey, S.D.; Drew, R.J. Shape and cost analysis of pressurized fabric structures for subsea compressed air energy storage. *Proc. Inst. Mech. Eng. Part C J. Mech. Eng. Sci.* **2011**, *225*, 1027–1043. [Google Scholar] [CrossRef]
12. Chen, L.; Wang, Y.; Xie, M.; Ye, K.; Mohtaram, S. Energy and exergy analysis of two modified adiabatic compressed air energy storage (A-CAES) system for cogeneration of power and cooling on the base of volatile fluid. *J. Energy Storage* **2021**, *42*, 103009. [Google Scholar] [CrossRef]
13. Rolland, K.J.; Nitsche, T.; Budt, M.; Doetsch, C. Isobaric storage of compressed air: Introduction of a novel concept based on phase change materials and pressure equalizing modules. *J. Energy Storage* **2023**, *61*, 106778. [Google Scholar] [CrossRef]
14. Assegie, M.A.; Siram, O.; Kalita, P.; Sahoo, N. Novel small-scale spring actuated scissor-jack assembled isobaric compressed air energy storage tank: Design analysis and simulation. *J. Energy Storage* **2024**, *89*, 111627. [Google Scholar] [CrossRef]
15. Zhang, X.; Xue, X.; Zhang, T.; Xie, N.; Wang, Y.; Ma, L.; Wang, G.; Mei, S.; Wen, J.; Gong, L. Thermodynamic and economic analysis of a novel gravity-enhanced compressed air energy storage system. *Energy Sci. Eng.* **2022**, *10*, 4044–4060. [Google Scholar] [CrossRef]
16. Guo, D.; Zhou, X.; Zhang, X.; Xu, Y.; Yin, Z.; Liu, C.; Fu, W.; Chen, H. Operation characteristics study of fiber reinforced composite air storage vessel for compressed air energy storage system. *J. Energy Storage* **2024**, *86*, 111148. [Google Scholar] [CrossRef]
17. Liu, H.; Liu, L.; Shi, M.; Jin, K.; Zhao, Y. Dynamic thermal characteristics of the air reservoir in a compressed air energy storage system during air charge and discharge processes. *Appl. Therm. Eng.* **2026**, *289*, 129891. [Google Scholar] [CrossRef]
18. Rutqvist, J.; Kim, H.-M.; Ryu, D.-W.; Synn, J.-H.; Song, W.-K. Modeling of coupled thermodynamic and geomechanical performance of underground compressed air energy storage in lined rock caverns. *Int. J. Rock Mech. Min. Sci.* **2012**, *52*, 71–81. [Google Scholar] [CrossRef]
19. Liao, J.; Jiang, Z.; Konietzky, H.; Huang, X.; Tian, X. A modified model considering air mixed convection for analyzing the thermodynamic and heat transfer processes in CAES caverns. *J. Energy Storage* **2025**, *136*, 118428. [Google Scholar] [CrossRef]
20. Menéndez, J.; Fernández-Oro, J.M.; Galdo, M.; Álvarez, L.; Bernardo-Sánchez, A. Numerical investigation of underground reservoirs in compressed air energy storage systems considering different operating conditions: Influence of thermodynamic performance on the energy balance and round-trip efficiency. *J. Energy Storage* **2022**, *46*, 103816. [Google Scholar] [CrossRef]
21. Di, S.; Tao, Z.; Huang, D.; Cheng, H.; Zhang, Y.; Zhang, Y. Numerical simulation on the evaluation of charging–storage–discharging thermodynamic process and long-term operation performance of compressed air energy storage rock cavern. *Energies* **2026**, *19*, 2120. [Google Scholar] [CrossRef]
22. Odukomaiya, A.; Abu-Heiba, A.; Gluesenkamp, K.R.; Abdelaziz, O.; Jackson, R.K.; Daniel, C.; Graham, S.; Momen, A.M. Thermal analysis of near-isothermal compressed gas energy storage system. *Appl. Energy* **2016**, *179*, 948–960. [Google Scholar] [CrossRef]

23. Odukomaiya, A.; Kokou, E.; Hussein, Z.; Abu-Heiba, A.; Graham, S.; Momen, A.M. Near-isothermal-isobaric compressed gas energy storage. *J. Energy Storage* **2017**, *12*, 276–287. [Google Scholar] [CrossRef]
24. Khaljani, M.; Vennard, A.; Harrison, J.; Surplus, D.; Murphy, A.; Mahmoudi, Y. Experimental and modelling analysis of efficiency enhancement in a liquid piston gas compressor using metal plate inserts for compressed air energy storage application. *J. Energy Storage* **2021**, *43*, 103240. [Google Scholar] [CrossRef]
25. Ni, W.; Hu, Y.; Li, Z. Operational stability control technology for gravity blocks in gravity compressed air energy storage systems. In *Hydropower and Renewable Energies*; Hu, Y., Sas, M., Jin, F., Zheng, S., Zhao, G., Eds.; Lecture Notes in Civil Engineering; Springer: Singapore, 2026; Volume 792, pp. 99–111. [Google Scholar] [CrossRef]
26. Richer, E.; Hurmuzlu, Y. A high performance pneumatic force actuator system: Part I—Nonlinear mathematical model. *J. Dyn. Syst. Meas. Control* **2000**, *122*, 416–425. [Google Scholar] [CrossRef]
27. Ka'ka, S.; Himran, S.; Renreng, I.; Sutresman, O. The pneumatic actuators as vertical dynamic load simulators on medium weighted wheel suspension mechanism. *J. Phys. Conf. Ser.* **2018**, *962*, 012022. [Google Scholar] [CrossRef]
28. Tada, S.; Yoshida, H.; Echigo, R.; Oishi, Y. A numerical analysis of the air in a cavern for the CAES-G/T. Laminar-model results compared with experiments. *Trans. Jpn. Soc. Mech. Eng. B* **1998**, *64*, 3830–3837. [Google Scholar] [CrossRef]

Disclaimer/Publisher's Note: The statements, opinions and data contained in all publications are solely those of the individual author(s) and contributor(s) and not of MDPI and/or the editor(s). MDPI and/or the editor(s) disclaim responsibility for any injury to people or property resulting from any ideas, methods, instructions or products referred to in the content.